submitted to *Icarus* 2/25/2000

Three-Dimensional Simulations of Mantle Convection in Io

Paul J. Tackley
Department of Earth and Space Sciences, University of California, Los Angeles

Gerald Schubert
Department of Earth and Space Sciences and Institute of Geophysics and Planetary Physics, University of California, Los Angeles

Gary A. Glatzmaier
Earth Sciences Department and Institute of Geophysics and Planetary Physics, University of California, Santa Cruz

Paul Schenk
Lunar and Planetary Institute, Houston, Texas

J. Todd Ratcliff
Jet Propulsion Laboratory, Pasadena, California

J-P. Matas
Ecole Normale Superiere, Lyon, France

Io has very high surface heat flow and an abundance of volcanic activity, which are thought to be driven by non-uniform tidal heating in its interior. This non-uniform heat is transported to the base of the lithosphere by very vigorous convection in Io's silicate mantle, the form of which is presumably responsible for the distribution of surface features such as volcanoes and mountains. We here present three-dimensional spherical calculations of mantle convection in Io, in order to ascertain the likely form of this convection and the resulting distribution of heat flow at the surface and core-mantle boundary. Different models of tidal dissipation are considered: the end-member scenarios identified by Ross and Schubert (1985) **of dissipation in the entire mantle, or dissipation in a thin (~100 km thick) asthenosphere, as well as the 'prefered' distribution of** Ross *et al*. (1990) **comprising 1/3 mantle and 2/3 asthenosphere heating. The thermal structure of Io's mantle and asthenosphere is found to be strongly dependent on tidal heating mode, as well as whether the mantle-asthenosphere boundary is permeable or impermeable. Results indicate a large-scale flow pattern dominated by the distribution of tidal heating, with superimposed small-scale asthenospheric instabilities that become more pronounced with increasing Rayleigh number. These small-scale instabilities spread out the surface heat flux, resulting in smaller heat flux variations with increasing Rayleigh number. Scaled to Io's Rayleigh number of O(10^{12}), variations of order a few percent are expected. This small but significant variation in surface heat flux may be compatible with the observed distributions of volcanic centers and mountains, which appear fairly uniform at first sight but display a discernible distribution when suitably processed. The observed distribution of volcanic centers is similar to the asthenosphere heating distribution, implying that most of the tidal heating in Io occurs in an asthenosphere.**

1. INTRODUCTION

The innermost Galilean satellites of Jupiter, Io, Europa and Ganymede, are in a Laplace resonance that maintains the satellites in non-circular orbits (e.g., (Peale 1999)). As a consequence of its nonzero eccentricity, the distance between Io and Jupiter and the overhead position of Jupiter in Io's sky vary periodically as Io orbits Jupiter. The resulting tidal deformation intensely heats Io (Peale *et al*. 1979, Yoder 1979, Schubert *et al*. 1981, Yoder and Peale 1981, Cassen *et al*. 1982, Ross and Schubert 1985, Ross and Schubert 1986, Schubert *et al*. 1986, Segatz *et al*. 1988) and drives the volcanic activity that has left its mark on every part of Io's surface. Io has been volcanically resurfaced in the recent geologic past, and beginning with Voyager, we have been witness to Io's ongoing volcanic activity (Morabito *et al*. 1979, Smith *et al*. 1979a, 1979b, Spencer and Schneider 1996, McEwen *et al*. 1998a, 1998b). Galileo observations of Io in the visible and near infrared have recorded volcanic plumes and lava flows with temperatures as high as about 1800 K (Stansberry *et al*. 1997, McEwen *et al*. 1998b, Lopes-Gautier *et al*. 1999); the high temperature lavas indicate that silicate volcanism is pervasive on Io (McEwen *et al.* 1998a, 1998b). Tidal dissipation deposits a prodigious amount of heat in Io; at least several times 10^{14} W is radiated to space from Io's hot surface (Veeder *et al*. 1994). Though Io is barely larger than Earth's Moon, it radiates energy at a rate that is at least an order of magnitude larger than the rate at which the entire Earth is cooling (Schubert *et al*. 2000).

The major questions about Io's thermal state relate to where in Io's interior the tidal heating is deposited and how the heat is transported to Io's surface. Two end-member

models of tidal dissipation have been explored by Segatz *et al*. (1988). In one model, tidal heating occurs in the deep mantle and is focused at the core-mantle boundary. It is known from measurements of Io's gravitational field (Anderson *et al.* 1996) and shape (Thomas *et al*. 1998) that Io has a metallic core whose radius may be as large as 50% of the satellite's radius. In the other model, tidal heating occurs in the shallow mantle and is focused at the upper and lower boundaries of a low viscosity, and perhaps partially molten, asthenosphere. It is not known if Io has an asthenosphere.

Clues to the nature of tidal dissipation inside Io have long been sought in the distribution of volcanic features on Io's surface (Carr *et al*. 1998) and in the topography of Io's surface (Ross *et al*. 1990). The possibility that surface observations might reveal the nature of tidal heating inside Io derives from differences in Io's surface heat flow pattern between the deep mantle heating model and the asthenosphere heating model. In the former model, surface heat flow maximizes at the poles, whereas in the latter model, surface heat flow has near equatorial maxima at the sub-Jovian and anti-Jovian longitudes and smaller local equatorial maxima at the orbit tangent longitudes. Accordingly, an equatorial preference of ongoing volcanic activity or surface volcanic features would imply an internal tidal heat source mainly in the asthenosphere, while a polar preference would suggest a heat source in the deep mantle. The predicted surface heat flow patterns are based on the assumption that tidally generated heat is transported radially upward to the surface. However, if mantle convection is the dominant heat transfer mechanism, it may smooth out the lateral spatial variations in internal heating and subdue or erase the pattern in the surface heat flow. This is one of the effects studied in the present paper.

Attempts to discern polar vs. equatorial concentrations of volcanic features on Io's surface have so far not led to convincing results because volcanic features such as calderas and flows are to be found everywhere. However, recent plume activity and locations of persistent hot spots seem to prefer the equator (Lopes-Gautier *et al.* 1999) and there are concentrations of bright spots and diffuse glows at the sub-Jovian and anti-Jovian points (McEwen *et al*. 1998). These observations support the asthenosphere heating model. A spatially-filtered view of Io's volcanic features and mountains, presented in this paper, is also suggestive of tidal heating mainly in an asthenosphere.

Large-scale longitudinal variations in Io's topography inferred from Voyager data were used by Ross *et al*. (1990) to constrain models of Io's internal structure and tidal dissipation. The Voyager topography had peaks and troughs in the equatorial region similar to the variations in surface heat flow from the asthenosphere heating model. Importantly, the heat flow peaks occurred in the topographic troughs. Ross *et al*. (1990) concluded that the topographic data were best fit by a model in which 2/3 of the tidal heating was deposited in an asthenosphere and 1/3 of the tidal heating was deposited in the deep mantle. The association of high heat flow with low topography required that the asthenosphere lie below a compositionally distinct, light lithosphere (or crust). The Voyager topography of Io has not been confirmed by Galileo observations (Thomas *et al.* 1998). Nevertheless, in this paper we adopt the internal structural and heating model of Ross *et al*. (1990) to study the nature of mantle convection in Io and its consequences for surface heat flow and volcanic activity. We also consider the end member models of all tidal heating in an asthenosphere and all tidal heating in the deep mantle.

2. MODEL AND PARAMETERS

The timescale for convective motions is much larger than the timescale associated with the periodic tidal flexing of Io on its 1.77 day orbit around Jupiter. Thus, for the purposes of modeling these convective motions, the mantle (including asthenosphere) and lithosphere of Io are assumed to be highly viscous fluids, and the infinite Prandtl number approximation, in which inertial terms in the momentum equation are ignored, is made. Due to the small size of Io, the effect of compressibility, as measured, for example, by the Dissipation number (Schubert *et al*. 2000), are expected to be negligible, so the Boussinesq approximation is also assumed. Viscous heating due to the convection is therefore also neglected. Thus the equations describing conservation of mass, momentum, and energy, plus the equation of state, are qualitatively the same as those used in previous studies of 3-D spherical convection applied to the mantles of Earth, Venus and Mars (e.g., (Machetel *et al.* 1986, Bercovici *et al*. 1989, Schubert *et al*. 1990, Glatzmaier and Schubert 1993, Schubert *et al*. 1993, Ratcliff *et al.* 1995)). The key new feature compared to previously-modeled planetary bodies is a three-dimensionally-varying tidal dissipation function discussed below.

The surface boundary is assumed to be rigid and isothermal. It is assumed that the core is fluid; thus the lower (core-mantle) boundary is assumed to be impermeable, shear-stress free, and isothermal. Furthermore, there is assumed to be zero net heat flux across the core-mantle boundary, corresponding to a core and mantle in thermal equilibrium, with no secular cooling. In spherical harmonic space this means that the spherically symmetric (ℓ=0) part of the radial temperature gradient vanishes at the core-mantle boundary. Note that the ℓ>0 parts of this gradient are not forced to vanish. Instead, we force the ℓ>0 parts of the temperature to vanish, since the fluid core below keeps the boundary essentially isothermal. However, the spherically symmetric part of the temperature is free to evolve with time.

The assumed model of tidal dissipation and related internal structure is based on that of Segatz *et al*. (1988) and Ross *et al*. (1990). We consider their idealized cases of all dissipation occurring in a ~100 km thick low-viscosity asthenosphere, or all dissipation occurring in a constant-viscosity mantle, as well as the preferred model of Ross *et al*. (1990) consisting of 2/3 asthenospheric heating plus 1/3 mantle heating. Their tidal dissipation distributions obtained by solving the relevant equations are here approximated using analytical functions, the horizontal forms of which are shown in Figure 1. In this figure, the sub- and anti-Jovian points correspond to 0° and 180° respectively. The appropriate three-dimensional tidal

dissipation function is imposed in the calculation as a heat source that is fixed in time, since the numerical timestep is large compared to the orbital period.

The internal structure of our model consists of a 100 km thick lithosphere/crust, a 100 km thick low-viscosity asthenosphere, and a 680 km thick mantle. Viscosity is a function of radius only, and is constant within each layer. The lithosphere/crust viscosity is 100 times higher than the viscosity in the mantle, whereas the viscosity in the asthenosphere is either the same as that in the mantle or 100 times lower than that in the mantle. Due to numerical limitations, this asthenospheric viscosity is not as low as that in the model of Ross *et al*. (1990), but two orders of magnitude reduction in viscosity should give some insight into the behavior induced by a low viscosity layer.

The internal mantle-asthenosphere boundary is assumed to be permeable in some cases but impermeable in other cases. An impermeable boundary is most consistent with the model of Ross *et al*. (1990), in which it was assumed that extreme differentiation of the mantle has made the mantle and asthenosphere chemically distinct with a density contrast large enough to prohibit intermixing. A permeable mantle-asthenosphere boundary corresponds to an Earth-like situation, in which the asthenosphere is mainly due to the close approach of the geotherm to the solidus, and possibly the presence of partial melt in some areas.

Suitable parameters for Io, based on an Fe-FeS core model (Segatz *et al*. 1988, Anderson *et al*. 1996), are given in Table 1.

TABLE I: Io's physical properties

Parameter	Symbol	Value	Units
Radius	R	1821.3	km
Core radius	R_c	941	km
Total mass	M	8.9327×10^{22}	kg
Mass of core	M_c	1.80161×10^{22}	kg
Mantle density	ρ	3270	kg/m^3
Total surface heat flow	H	10^{14}	W
Surface heat flux	F	2.4	W/m^2
Surface temperature	T_{surf}	100	K
Average tidal dissipation	$<Q>$	1.4023×10^{-9}	W/kg
Lithosphere thickness	D_{lith}	100	km
Asthenosphere thickness	D_{asth}	100	km
Gravitational acceleration	g	1.8	m/s^2
Heat capacity	c_p	1200	J kg^{-1} K^{-1}
Thermal diffusivity	κ	1.0×10^{-6}	m^2/s
Thermal expansivity	α	3×10^{-5}	K^{-1}
Mantle viscosity	η_{mantle}	10^{16}-4×10^{17}	Pa s
Asthenosphere viscosity	η_{asth}	10^8 - 10^{12}	Pa s

It is not possible using presently available resources to simulate convection in Io in 3-D spherical geometry at the convective vigor that would result from the parameters in Table 1. A common measure of the convective vigor is the Rayleigh number, which for the case of pure internal heating is given by:

$$Ra_H = \frac{\rho g \alpha < Q > D^5}{\eta c_p \kappa^2} \qquad (1)$$

For the parameters listed in Table 1, and using the mantle viscosity that is assumed to be 10^{17} Pa s, Ra_H=1.09x10^{12}, approximately 4 orders of magnitude higher than that which can presently be simulated. Thus, it is necessary to scale some parameters to reduce Ra_H. A scaling is chosen that maintains the correct heat flux and internal temperatures by adjusting (increasing) viscosity η and thermal diffusivity κ. Appropriate adjustments for these parameters can be derived by remembering that, for internally-heated convection, the Nusselt number Nu is given by:

$$Nu = \frac{\Delta T_{scale}}{\Delta T_{actual}} \text{ where } \Delta T_{scale} = \frac{< Q > D^2}{c_p \kappa} \qquad (2)$$

and ΔT_{actual} is the temperature increase across the system. Nu scales roughly as:

$$Nu \quad Ra_H^{1/4} \qquad (3)$$

We wish to keep ΔT_{actual} constant while varying Ra_H (hence Nu) for fixed tidal heating rate $<Q>$. This can best be accomplished by adjusting κ to scale ΔT_{scale},

$$\frac{\kappa_{Model}}{\kappa_{Io}} = \left(\frac{Ra_{H,Model}}{Ra_{H,Io}} \right)^{-1/4} \qquad (4)$$

and η to account for the remainder of the change in Ra_H.

$$\frac{\eta_{Model}}{\eta_{Io}} = \left(\frac{Ra_{H,Model}}{Ra_{H,Io}} \right)^{-1/2} \qquad (5)$$

Another parameter adjustment must be made to account for magmatic heat transport through the lithosphere, which is thought to account for most of the heat transfer across the lithosphere. Thus, κ_{lith} in the lithospheric layer is really an 'effective' value that represents this process; this representation is crude because a conductive, rather than a 'magmatic resurfacing', temperature profile will be obtained. A suitable value for κ_{lith} should lead to reasonable interior temperatures, i.e., a temperature rise across the lithosphere ΔT_{lith} of about 1200 K. Based on a conductive temperature profile this can be estimated as

$$\kappa_{lith} = \frac{D_{lith} F}{\rho c_p \Delta T_{lith}} . \qquad (6)$$

From the values in Table 1, we get κ_{lith}=5x10^{-5} m^2/s. This value is not scaled with Ra_H as is κ in the asthenosphere and mantle, because the parameters in the above equation do not change with Ra_H.

Cases

From the preceding discussion, it can be seen that four parameters are changed: the Rayleigh number (varied over 3 orders of magnitude), tidal dissipation mode (mantle, asthenosphere or combined), mantle-asthenosphere boundary (permeable or impermeable), and the asthenosphere viscosity (same as mantle or 100 times lower). The following parameter combinations are presented:

Table II. Presented Cases.

Case	Ra_H	Heating	M-A bndry	$\eta_{asth}/\eta_{mantle}$
1	2.5×10^4	M	P	0.01
2	2.5×10^7	M	P	0.01
3	2.5×10^4	A	P	0.01
4	2.5×10^7	A	P	0.01
5	2.5×10^4	MA	P	0.01
6	2.5×10^5	MA	P	0.01
7	2.5×10^6	MA	P	0.01
8	2.5×10^7	MA	P	0.01
9	2.5×10^6	MA	I	0.01
10	2.5×10^7	MA	I	0.01
11	2.5×10^7	MA	P	1.0

M=mantle, A=asthenosphere, MA=combined, P=permeable, I=impermeable

In the above table, Ra_H is calculated using the mantle viscosity. The volume-averaged $<Ra_H>$ is about 20 times higher in the cases with a low-viscosity asthenosphere, and 8% lower in the case with a same-viscosity asthenosphere (because of the high-viscosity lithosphere).

Numerical Method

Solutions are obtained via a spectral transform method previously described in detail elsewhere (Glatzmaier 1988, Tackley *et al.* 1994). To summarize, variables are expanded in spherical harmonics azimuthally and Chebyshev polynomials radially. Three separate Chebyshev domains are used, representing the lithosphere, asthenosphere and mantle, respectively. The use of separate Chebyshev expansions matched by continuity of velocity and stress at the interfaces, as used in some previous studies using this code (Glatzmaier and Schubert 1993, Tackley *et al*. 1993, 1994), allows the different layers to have quite different physical properties such as viscosity and thermal conductivity, and also provides enhanced radial resolution at the surface, the core-mantle boundary and the two internal boundaries. In addition, internal boundaries can be made impermeable if desired. The resolution used depends on the Rayleigh number. Radial resolution is either 33 Chebyshev levels in the mantle, 13 in the asthenosphere and 13 in the lithosphere (59 in total), or 49 levels in the mantle and 21 levels in each of the asthenosphere and lithosphere (91 in total). Azimuthally, the spherical harmonic truncation between 31 and 191 was used (corresponding to between 96 and 576 points around the equator).

The numerical method is parallelized and solutions were run on a "Beowulf" cluster of Pentium II PCs running Linux and communicating using the MPI library. Cases were started from either random conditions or a case with similar parameters and run until statistical equilibrium was reached, at least 10,000 time steps and often more.

3. RESULTS

Effect of heating mode and Ra

Cases with either all-mantle heating or all-asthenosphere heating are illustrated in Figure 2. The central point in the image is at latitude 30° N, longitude 20° E; thus the sub-Jovian point is to the lower left of the image center. At low *Ra* (top row), the convective patterns are steady-state and basically reflect the tidal dissipation distribution shown in Figure 1. With pure mantle heating (parts a. and b.), there are upwellings at the poles and a downwelling around the equator. The polar upwellings are not axisymmetric but have a shape that reflects the tidal dissipation distribution.

With pure asthenosphere heating (parts c. and d.), there are two major asthenospheric upwelling lobes centered around the equator, with two minor ones inbetween, reflecting the tidal heating distribution. Downwellings occur inbetween these, but the major downwellings are at the two poles, opposite to the situation with pure mantle heating, where upwellings occur at the poles.

At a Rayleigh number 3 orders of magnitude higher (bottom row), the temperature structure and overall flow pattern are very similar to those at the lower *Ra*, but superimposed on them are small-scale, time-dependent instabilities. The persistence of the large-scale structure with increasing *Ra* is encouraging for applying these results to Io, with its much higher *Ra*.

The temperature structure at high *Ra* may be further elucidated by studying cross-sectional and constant-radius slices (Figure 3a.-h.). It can be seen that most of the temperature contrast in the system occurs across the lithosphere. In the mantle-heating case (Figure 3 a. b. e. f.), the major polar upwellings are the dominant features, but the lower viscosity of the asthenosphere is evident from the small-scale instabilities that develop in that region. In the asthenosphere heating case (parts c. d. g. h.), the asthenosphere is clearly hotter than the underlying mantle region, in most places. The small-scale instabilities tend to look more point-like, rather than linear as the isosurfaces tend to emphasize. The major cold downwellings do appear to penetrate into the mantle, to some extent.

In the asthenosphere-heating case the mantle receives zero net heat from the core and no internal tidal heating, so it is interesting to ascertain whether there is any circulation in the mantle, and what temperature it adopts. There will inevitably be some circulation induced by a combination of mechanical and thermal coupling with the overlying asthenosphere. Mechanical coupling should be made small by the viscosity contrast. Thermal coupling will warm thin regions at the top of the mantle that are under areas of hot asthenosphere. These

warm mantle regions will then tend to rise up into the asthenosphere (assuming a permeable boundary), inducing some circulation in the rest of the mantle. Regarding the horizontally-averaged temperature, the mantle is stably stratified on average, with coldest material at the bottom. What determines this equilibrium state? The mantle cannot get too warm because then, downwellings from the asthenosphere would penetrate it, and cool it down. On the other hand, the second law of thermodynamics prevents the mantle from becoming colder than the coldest asthenospheric downwellings. Indeed, the mantle is slowly warmed over very long time scales by thermal diffusion from above. Thus, the equilibrium state will be a balance between this conductive warming and cooling by asthenospheric downwellings.

The combined heating case (2/3 asthenosphere, 1/3 mantle) results in an interesting compromise between the two flow patterns that is clearest at low *Ra* (Figure 4a. and b.). The asthenospheric polar downwellings dominate the mantle polar upwelling, diverting the polar upwelling into a ring around the polar region. In the asthenosphere this diverted mantle upwelling combines with the asthenospheric upwellings to give an expression that is quite different from the purely asthenospheric mode, in two ways: (i) the symmetry around the equator is virtually 4-fold, rather than 2-fold, and (ii) upwellings are focused in lobes North and South of the equator, whereas with pure asthenospheric heating the upwellings form large patches straddling the equator. Thus, it is clear that the effect of combining the two heating modes cannot be predicted by simply adding the temperature distribution from each mode in isolation, because they strongly modulate each other.

The effect of *Ra* on the results is most clearly indicated by Figure 4, which shows results for the same model but at 4 different Rayleigh numbers increasing downward in order of magnitude steps. As *Ra* is increased, the upwellings and downwellings develop small-scale instabilities. These instabilities are initially linear and aligned with the flow direction, which is expected from studies on the development of instabilities in a shear flow (Richter 1973, Richter and Parsons 1975), and which may occur underneath oceanic plates on Earth. As *Ra* is increased these linear instabilities break up further and start to develop a more point-like nature. It is expected that if *Ra* were increased further, point-like rather than linear instabilities would be dominant.

The highest-*Ra* case can be further examined by looking at temperature slices (Figure 3 i. j. m. n.). In these views, the small-scale modes are seen to be restricted to the asthenosphere, and are visible both in the slices and in constant-radius sections, in which they look very point-like. In these views the major upwellings look quite narrow, which is interesting because they arise from distributed heating rather than a focused boundary layer.

Impermeable Mantle-Asthenosphere Boundary

An impermeable mantle-asthenosphere is most consistent with the model of Ross *et al*. (1990), as discussed earlier. The impermeable boundary makes a large difference to the flow pattern, as shown in two cases illustrated in Figure 5. At the lower *Ra* (parts a. b.), the temperature structure in the mantle looks like that obtained with pure mantle heating, with upwellings at the poles and downwellings at the equator. Likewise, the temperature structure in the asthenosphere looks similar to that obtained with pure asthenospheric heating. Thus, both regions are able to exhibit their preferred flow pattern, which is not the case with a permeable boundary. The coupling between the layers is dominantly mechanical, with upwellings in one layer (for example, at the poles in the mantle) associated with downwellings in the other layer (at the poles in the asthenosphere).

However, at the highest *Ra* (Figure 5 parts c. and d.), the flow pattern appears more complex, particularly in the mantle where the strong polar upwelling and equatorial downwelling are not evident, although there still seem to be more mantle downwellings near the equator than near the poles. Mechanical coupling is still evident, for example the north to south downwelling near the center for part c., but apparently thermal coupling plays a greater role.

Figure 3k.,l.,o.,p. show slices through this higher-*Ra* model. There is clearly a large temperature difference between the asthenosphere and mantle, due to the presence of an internal boundary layer. The asthenospheric temperature distribution (part o.) resembles the asthenosphere heating distribution, whereas the mantle seems fairly uniformly hot, with scattered downwellings that are more prevalent near the equator.

Previous work on layered convection indicates a preference for mechanical coupling when the viscosity contrast between the layers is small but thermal coupling when the viscosity contrast between the layers is large (Olson 1984, Cserepes and Rabinowicz 1985, Ellsworth and Schubert 1988, Glatzmaier and Schubert 1993). The presented results have an intermediate viscosity contrast, but the real viscosity contrast in Io may be much higher, implying thermal coupling.

Effect of asthenosphere viscosity

What effect does the low viscosity of the asthenosphere have? To gain some insight into this question, a case is presented in which the asthenosphere has the same viscosity as the mantle, rather than a 100 times lower viscosity. The results, illustrated in Figure 5 e. f., should be compared to the Figure 4 g. h., which has the same mantle and lithospheric viscosity but 1/100 the asthenospheric viscosity. The large-scale temperature distribution looks similar, but small-scale instabilities are less prevalent and are not restricted to the asthenosphere in the case with the same asthenosphere and mantle viscosity. Thus, the main effect of lower asthenospheric viscosity seems to be to promote small-scale convective instabilities. In Io the viscosity contrast between mantle and asthenosphere may be higher.

Temperature Profiles

Figure 6 shows geotherms for the 5 cases at the highest Rayleigh number. In all cases, there is a large, linear temperature gradient across the lithosphere. The mantle-heating case displays a slight temperature rise near the CMB and a temperature drop from mantle to asthenosphere, which is probably due to the more efficient heat transport in the low-viscosity asthenosphere. The asthenospheric-heating case displays a subadiabatic mantle, with a peak temperature in the asthenosphere due to the tidal heating. The combined heating case shows characteristics of both of these cases. With an impermeable mantle-asthenosphere boundary, the lower mantle is much hotter than the asthenosphere due to the internal boundary layer that forms to conduct heat across this boundary. With a high-viscosity asthenosphere, the whole interior is substantially hotter, indicating the importance of the low-viscosity asthenosphere in improving heat transport.

Surface and CMB heat flux variations

The distribution of surface heat flow is probably the most useful property of these simulations that can be related to observables like volcanism, topography and mountains. The heterogeneous heat flow across the CMB may be responsible for driving circulation in a fluid core, which may induce a magnetic field, some evidence for which was obtained by Galileo magnetometer measurements (Kivelson *et al*. 1996). Thus, it is important to assess which cases give surface heat flows that are compatible with observations, and how the heat flow distributions scale with *Ra*. It was previously assumed (Ross *et al*. 1990) that heat flow would occur directly above heat production. In Io, the lithospheric heat flow is thought to be accommodated by magmatic transport, whereas in these calculations, heat is transported through the lithosphere by conduction, which may produce an unrealistic 'filtering' of heat flux variations. Thus, we consider the variation of heat flux into the base of the lithosphere, as well as heat flux at the outer surface.

Figure 7 shows the effect of Rayleigh number on heat flux through the surface, base of lithosphere and CMB for cases with the combined heating distribution. These have been time-averaged over the last half of each run to integrate over time-dependent small-scale instabilities. Plots show heat flux variations relative to the average, which is about 2.4 W/m^2 for the surface but 0 for the CMB.

The surface heat flow variation clearly shows the 8 distinct maxima, with 4 maxima going around the equator and 2 going from pole to pole. As *Ra* is increased, heat flux variation is reduced, while a more focused pattern of almost linear high-heat-flux anomalies appears. These linear features can be attributed to the 'deflected' mantle heating. The reduction in heat flow variation is due to the spreading-out of anomalies by small-scale convection. The heat flow into the base of the lithosphere looks similar to the surface heat flow at low *Ra*, but displays an increasing amount of small scale structure as *Ra* is increased. This small-scale structure is associated with the small-scale asthenospheric instabilities, and does not appear in the surface heat flux distributions because the (mostly conductive) lithosphere acts as a filter to short-wavelength structure. The CMB has heat flux variations that are larger than surface heat flux variations by a factor of ~2, with a cubic arrangement of peaks, four around the equator and two at the poles. These peaks correspond to the positions of downwellings. The pattern of CMB heat flux anomalies is approximately opposite to the pattern of surface heat flux anomalies.

The effects of other physical characteristics are show in Figure 8 for the highest-Ra cases. With mantle-only heating, surface and base of lithosphere heat flux maxima occur at the poles, whereas CMB heat flux maxima occur in two places at the equator, with the two patterns again being anticorrelated. With asthenosphere-only heating, the surface and base of lithosphere heat flux distributions resemble the heating distribution, whereas at the CMB, heat flux variations are negligible at the scale being plotted. With an impermeable mantle-asthenosphere boundary, the surface and base of lithosphere heat flux patterns also resemble the asthenospheric heating pattern, whereas the CMB high heat flow is concentrated around the equator, consistent with mantle heating. It is interesting that in this case the asthenospheric instabilities (visible in the base of lithosphere heat flux distribution) appear to be fully three-dimensional, rather than the linear instabilities observed with a permeable asthenosphere:mantle boundary. A same-viscosity asthenosphere leads to heat flow similar to that of the combined heating, but with smaller peaks at the poles and asthenospheric instabilities with a slightly larger scale.

How can the *Ra* trend be extrapolated to Io's Rayleigh number? Figure 9 shows how peak-to-peak and rms. (i.e., standard deviation) heat flux variation scale with *Ra* for the four combined-heating cases illustrated in Figure 7. Surface, base of lithosphere and CMB fluxes are considered. For the boundary fluxes (surface and CMB), all measures of heat flux variation appear to scale in approximately the same way, although the lines are not perfectly linear. The base of lithosphere flux scales differently, with peak-to-peak variation being almost constant, and rms. variation decreasing with *Ra* slower than the rms. variation of boundary fluxes. With the assumption of a power-law relationship

$$\Delta F \quad Ra_H^{\beta}, \tag{7}$$

where ΔF is the variation in surface heat flux, least-squares fits to the four boundary flux lines yield exponents β between -0.144 and -0.226, with an average of -0.189. This exponent is close to the value of -0.2 obtained in a related study in Cartesian geometry (P.J. Tackley, manuscript in preparation). Exponents for the base of lithosphere lines are -0.107 for the rms. variation and 0.001 for the peak-to-peak variation, with an average of all 6 lines being -0.144.

With these exponents, heat flux variations can be scaled from the highest Rayleigh number in this study (2.5×10^7) to the Rayleigh number of Io ($\sim10^{12}$), a difference of about 4.5 orders of magnitude. However, due to the difference between the scaling of heat flux variations at the surface and base of lithosphere, there is some uncertainty in this extrapolation. From Figure 7 it is clear that the larger variations in base of

lithosphere heat flux are associated with increasingly small-scale structure as *Ra* is increased, so for the purposes of relating heat flux to large-scale distributions of surface features, some degree of long-wavelength filtering (as obtained, for example, by considering surface heat flux) may be appropriate. Taking the surface scaling exponent β of -0.2 leads to a further reduction in heat flux variation by a factor of ~8. Thus, a surface peak-to-peak variation of 0.4 W/m^2 (read from Figure 9) would be reduced to 0.05 W/m^2 for Io, a variation of about 2% of the mean surface heat flux. With an impermeable mantle-asthenosphere boundary (case 10, Figure 8, 3rd row), the surface heat flux variations are somewhat larger, so 2% should be regarded as a lower bound. Taking the scalings for base of lithosphere heat flux variations, peak variation should remain roughly constant, and rms. variation (β=-0.1) should be reduced by a factor of ~3, falling from 0.3 W/m^2 to 0.1 W/m^2, a variation of about 4% of the mean surface heat flux. In conclusion, a surface heat flux variation of a few percent is expected at Io's convective vigor.

What variations in CMB heat flux are expected? The peak-to-peak variation of ~0.7 W/m^2 read from Figure 9 for the highest Rayleigh number of 2.5x10^7 would scale to ~0.09 W/m^2 at Io's convective vigor.

Comparison with surface observations

The surface of Io is dominated by two major landforms: volcanic centers and mountains. The distribution of both could be influenced by internal convection; volcanic centers could be localized over rising asthenosphere, mountains and rifts could form over zones of compression or extension in the overlying crust. The roughly 60 currently active volcanic hotspots (as detected by Voyager and Galileo) appear to be more or less uniformly distributed over the surface, although they might occur less frequently in whitish, SO_2-rich areas (Lopes-Gautier *et al*. 1999). Persistently active hotspots tend to be distributed in equatorial regions, however, which Lopes-Gautier *et al*. (1999) suggested was more compatible with asthenospheric tidal dissipation.

There are over 300 active and inactive volcanic centers, including calderas, flow-fields, shield volcanoes, and plume vents. These presumably provide a more integrated record of volcanic activity on Io over geologic time. Carr *et al*. (1998) report a global asymmetry in the distribution of volcanic centers, with weak antipodal concentrations near 0° and 180° longitude. Unpublished global surveys by Schenk and Hargitai (1998, in preparation 2000) also support such a distribution (Figure 10a). Global maps of volcanos on Io are subject to a variety of biases. The recognition of discrete volcanic centers can be difficult near the poles and on surfaces obscured by recent plume deposits. It is noted that both studies used Galileo nominal mission data to map volcanoes over the anti-Jovian hemisphere, which are still a factor 2-3 poorer in resolution than Voyager imaging over the sub-Jovian hemisphere. Addition of Galileo GEM data over these regions, with resolutions comparable to Voyager, should improve the robustness of this conclusion.

Although the origins of Io's 100 or so mountains are unclear, most are non-volcanic and many appear to be tilted fault blocks (Carr *et al*. 1998, Schenk and Bulmer 1998). No obvious distribution pattern, such as linear or arcuate ranges, has been detected to suggest that mountains on Io are linked to an internal convection pattern. Rather, the choice seems to be whether the formation of mountains on Io is secondarily influenced by internal dynamics. Using Galileo nominal mission data, Carr *et al*. (1998) concluded that mountains are essentially randomly distributed on the surface. Using Voyager stereo data in combination with Galileo nominal and GEM data, Schenk and Hargitai (1998) find a distinctly asymmetric distribution (Figure 10b). The two areas with the greatest areal concentrations of mountains are centered near 90º and 270º longitude, located 90º in longitude from the apparent volcanic concentration areas. Galileo GEM data analysis (Schenk and Hargitai, manuscript in preparation) strengthens these conclusions.

The distribution patterns of mountains and volcanoes, however preliminary, suggest a relatively simple internal heating and convection pattern within Io's mantle, consistent with the 3-D convection models. The distribution pattern of volcanoes on Io (Figure 10a) resembles the asthenospheric heating pattern (Figure 1a), suggesting that asthenospheric heating is the dominant tidal heating mode in Io. Surface heat flux distributions for cases with all or 2/3 asthenosphere heating in Figure 8, also resemble the asthenosphere heating distribution. However, surface heat flux distributions for cases with 2/3 asthenosphere heating and a permeable asthenosphere:mantle boundary (Figure 7), are slightly different from the asthenosphere heating distribution, due to the heat input from 'deflected' polar upwellings, as discussed earlier. Thus, it appears that either pure asthenosphere heating, or mixed heating with in impermeable asthenosphere:mantle boundary, provide the best match to surface observations. The links between mountain formation and collapse, regional volcanic activity, and mountain burial are not well understood, however, and further Galileo GEM data analysis should prove illuminating.

4. DISCUSSION AND CONCLUSIONS

The results presented here show that the thermal structure of Io's mantle and asthenosphere is strongly dependent on tidal heating mode, as well as other physical characteristics such as whether the mantle-asthenosphere boundary is permeable or impermeable. Models with only mantle heating or only asthenosphere heating display thermal structures and boundary heat flux distributions that closely resemble the tidal heating distribution. Mantle heating produces upwellings at the poles and downwellings at the equator, whereas asthenosphere heating produces downwellings at the poles and a low-latitude pattern of upwellings and downwellings that resembles the tidal heating distribution, with two major hot lobes facing towards and away from Jupiter. With only asthenosphere heating, the mantle is stably stratified on average with very subdued temperature variations, an overall temperature similar to the coldest

regions in the asthenosphere, and flows driven by a combination of thermal and mechanical coupling to the asthenosphere.

With combined heating based on the 'preferred' model of Ross *et al.* (1990), the asthenospheric polar downwellings deflect the mantle polar upwellings to lower latitudes, resulting in a thermal structure and heat flow pattern that has eight distinct maxima, two in the pole-to-pole direction and four in the equatorial direction. If the mantle-asthenosphere boundary is, however, impermeable, the structures in the mantle and asthenosphere again come to resemble the respective heating distributions, with dominantly mechanical coupling between the layers, although this may revert to thermal coupling if the viscosity contrast were larger.

As Rayleigh number is increased, the large-scale structure remains stable, but small-scale asthenospheric instabilities become increasingly pronounced, and transition from linear to point-like as Rayleigh number is increased. Lower asthenospheric viscosity accentuates these small-scale instabilities. The presented results cover 3 orders of magnitude in Rayleigh number, but are still 4 orders of magnitude in Rayleigh number lower than the real Io. It may be that the observed trend can be simply extrapolated to Io, however, it is sometimes the case in fluid dynamical situations that the system undergoes transitions in behavior as a parameter is changed, rather than changing smoothly. For example, a transition to turbulent and then to 'hard turbulent' convection has been documented in infinite-Prandtl-number fluids (Hansen *et al*. 1990, Yuen *et al*. 1993, Travis and Olson 1994). Additional transitions may occur at even higher Rayleigh numbers (Vincent and Yuen 1999).

The small-scale convection spreads out the surface heat flux so that variations are much smaller than that predicted by simple vertical heat transport, although the pattern looks similar to the tidal heating distribution. Interpolating to Io's convective regime, heat flux variations are estimated to be small, of order a few percent. This may be consistent with observations of the distribution of surface volcanism and mountains, which at first glance seem fairly uniformly (randomly) distributed, but after analysis, display a distribution that somewhat resembles the asthenospheric heating pattern, with a maximum at the equator and two repetitions of the pattern in the longitudinal direction (i.e., a wavelength of 180°). This symmetry constrains the model to be either all-asthenospheric heating, or combined heating with an impermeable mantle-asthenosphere boundary, i.e., the model of Ross *et al*. (1990).

We have based our interior structure and tidal dissipation model on that developed in a series of papers (Ross and Schubert 1985, Ross and Schubert 1986, Segatz *et al*. 1988, Ross *et al*. 1990), and concluded that the preferred model in the latter paper may provide a reasonable fit to observations. It is possible, however, to imagine different interior structure models (e.g., Keszthelyi *et al.* (1999)). For example, rather than having a distinct asthenosphere and mantle with a jump in viscosity between them, it is possible that viscosity could increase smoothly with depth by several orders of magnitude, due to a smooth decrease in percentage of partial melt. Of course, any interior structure model must be capable of generating the observed surface heat flux, and no one has yet investigated the tidal dissipation that would result from a model with a smooth viscosity profile. Thus, consideration of such models is deferred to future studies that should also simulate tidal dissipation.

There are several other physical complexities that are neglected in the present study and should be modeled in the future. Lateral variations in viscosity (and elastic modulus) arising from lateral temperature variations, should be represented, although this may be a small effect in the asthenosphere where its low viscosity would allow only small lateral temperature variations. However, in reality there will be a two-way feedback in which viscosity variations due to convection affect the distribution of tidal heating, which in turn affects the convection. This may result in nonlinear behavior, which results in very time-dependent heating and convection (Ojakangas and Stevenson 1986). Io's interior may also contain large percentages of partial melt (Keszthelyi *et al*. 1999), which introduces dynamical complexities such as melt-solid segregation (McKenzie 1984, Richter and McKenzie 1984, Scott and Stevenson 1984, Scott and Stevenson 1986).

Acknowledgments. Supported by the David and Lucile Packard Foundation, NASA grants NAG5-3863, NAG5-8066, The University of California's Visiting Scholar and Research Partnership Initiative programs and the NSF Geophysics Program through grant EAR-9902969.

REFERENCES

Anderson, J. D., W. L. Sjogren and G. Schubert 1996. Galileo gravity results and the internal structure of Io. *Science* 272, 709-12.

Bercovici, D., G. Schubert, G. A. Glatzmaier and A. Zebib 1989. 3-Dimensional Thermal-Convection In a Spherical-Shell. *Journal Of Fluid Mechanics* 206, 75-104.

Carr, M. H., A. S. McEwen, K. A. Howard, F. C. Chuang, P. Thomas, P. Schuster, J. Oberst, G. Neukum and G. Schubert 1998. Mountains and calderas on Io: possible implications for lithosphere structure and magma generation. *Icarus* 135, 146-65.

Cassen, P. M., S. J. Peale and R. T. Reynolds 1982. Structure and thermal evolution of the Galilean satellites, in *Satellites of Jupiter*, edited by D. Morrison, pp. 93-128, The University of Arizona Press, Tucson.

Cserepes, L. and M. Rabinowicz 1985. Gravity and Convection In a 2-Layer Mantle. *Earth and Planetary Science Letters* 76, 193-207.

Ellsworth, K. and G. Schubert 1988. Numerical-Models Of Thermally and Mechanically Coupled 2-Layer Convection Of Highly Viscous Fluids. *Geophysical Journal Oxford* 93, 347-363.

Glatzmaier, G. A. 1988. Numerical Simulations Of Mantle Convection - Time-Dependent, 3-Dimensional, Compressible, Spherical-Shell. *Geophysical and Astrophysical Fluid Dynamics* 43, 223-264.

Glatzmaier, G. A. and G. Schubert 1993. 3-Dimensional Spherical-Models Of Layered and Whole Mantle Convection. *Journal Of Geophysical Research-Solid Earth* 98, 21969-21976.

Hansen, U., D. A. Yuen and S. E. Kroening 1990. Transition to Hard Turbulence In Thermal-Convection At Infinite Prandtl Number. *Physics Of Fluids a-Fluid Dynamics* 2, 2157-2163.

Keszthelyi, L., A. S. McEwen and G. J. Taylor 1999. Revisiting the hypothesis of a mushy global magma ocean in Io. *Icarus* 141, 415-19.

Kivelson, M. G., K. K. Khurana, R. J. Walker, J. Warnecke, C. T. Russell, J. A. Linker, D. J. Southwood and C. Polanskey 1996. Io's interaction with the plasma torus: Galileo magnetometer report. *Science* 274, 396-8.

Lopes-Gautier, R., A. S. McEwen, W. B. Smythe, P. E. Geissler, L. Kamp, A. G. Davies, J. R. Spencer, L. Keszthelyi, R. Carlson, F. E. Leader, R. Mehlman and L. Soderblom 1999. Active volcanism on Io: global distribution and variations in activity. *Icarus* 140, 243-64.

Machetel, P., M. Rabinowicz and P. Bernardet 1986. 3-Dimensional Convection In Spherical-Shells. *Geophysical and Astrophysical Fluid Dynamics* 37, 57-84.

McEwen, A. S., L. Keszthelyi, P. Geissler, D. P. Simonelli, M. H. Carr, T. V. Johnson, K. P. Klaasen, H. H. Breneman, T. J. Jones, J. M. Kaufman, K. P. Magee, D. A. Senske, M. J. S. Belton and G. Schubert 1998a. Active volcanism on Io as seen by Galileo SSI. *Icarus* 135, 181-219.

McEwen, A. S., L. Keszthelyi, J. R. Spencer, G. Schubert, D. L. Matson, R. Lopesgautier, K. P. Klassen, T. V. Johnson, J. W. Head, P. Geissler, S. Fagents, A. G. Davies, M. H. Carr, H. H. Breneman and M. J. S. Belton 1998b. High-temperature silicate volcanism on Jupiter's moon Io. *Science* 281, 87-90.

McKenzie, D. 1984. The Generation and Compaction Of Partially Molten Rock. *Journal Of Petrology* 25, 713-765.

Morabito, L. A., S. P. Synnott, P. N. Kupferman and S. A. Collins 1979. Discovery of currently active extraterrestrial volcanism. *Science* 204, 972.

Ojakangas, G. W. and D. J. Stevenson 1986. Episodic volcanism of tidally heated satellites with application to Io. 66,

Olson, P. 1984. An Experimental Approach to Thermal-Convection In a 2-Layered Mantle. *Journal Of Geophysical Research* 89, 1293-1301.

Peale, S. J. 1999. Origin and evolution of the natural satellites. *Ann. Rev. Astron. Astrophys.* 37, 533-602.

Peale, S. J., P. Cassen and R. T. Reynolds 1979. Melting of Io by tidal dissipation. *Science* 203, . 892-894.

Ratcliff, J. T., G. Schubert and A. Zebib 1995. 3-Dimensional Variable Viscosity Convection Of an Infinite Prandtl Number Boussinesq Fluid In a Spherical-Shell. *Geophysical Research Letters* 22, 2227-2230.

Richter, F. M. 1973. Convection and the large-scale circulation of the mantle. *J. Geophys. Res.* 78, 8735-8745.

Richter, F. M. and D. McKenzie 1984. Dynamical Models For Melt Segregation From a Deformable Matrix. *Journal Of Geology* 92, 729-740.

Richter, F. M. and B. Parsons 1975. On the interaction of two scales of convection in the mantle. *J. Geophys. Res.* 80, 2529-41.

Ross, M. and G. Schubert 1986. Tidal dissipation in a viscoelastic planet. *J. Geophys. Res.* 91, 447-52.

Ross, M. N. and G. Schubert 1985. Tidally forced viscous heating in a partially molten Io. *Icarus* 64, 391-400.

Ross, M. N., G. Schubert, T. Spohn and R. W. Gaskell 1990. Internal structure of Io and the global distribution of its topography. *Icarus* 85, 309-25.

Schenk, P. M. and M. H. Bulmer 1998. Origin of mountains on Io by thrust faulting and large-scale mass movements. *Science* 279, 1514-17.

Schubert, G., D. Bercovici and G. A. Glatzmaier 1990. Mantle Dynamics In Mars and Venus - Influence Of an Immobile Lithosphere On 3-Dimensional Mantle Convection. *Journal Of Geophysical Research-Solid Earth and Planets* 95, 14105-14129.

Schubert, G., G. A. Glatzmaier and B. Travis 1993. Steady, 3-Dimensional, Internally Heated Convection. *Physics Of Fluids a-Fluid Dynamics* 5, 1928-1932.

Schubert, G., T. Spohn and R. T. Reynolds 1986. Thermal histories, compositions and internal structures of the moons of the solar system, in *Satellites*, edited by J. A. Burns and M. S. Matthews, pp. 224-292, The University of Arizona Press, Tucson.

Schubert, G., D. J. Stevenson and K. Ellsworth 1981. Internal structures of the Galilean satellites. *Icarus* 47, . 46-59.

Schubert, G., D. L. Turcotte and P. Olson 2000. Mantle Convection in the Earth and Planets, Cambridge University Press.

Scott, D. R. and D. J. Stevenson 1984. Magma solitons. *Geophys. Res. Lett.* 11, 1161-4.

Scott, D. R. and D. J. Stevenson 1986. Magma ascent by porous flow. *J. Geophys. Res.* 91, 9283-96.

Segatz, M., T. Spohn, M. N. Ross and G. Schubert 1988. Tidal dissipation, surface heat flow, and figure of viscoelastic models of Io. *Icarus* 75, 187-206.

Smith, B. A., J. McCauley, D. Morrison, T. Owen, C. Sagan, E. M. Shoemaker, R. Strom, V. E. Suomi, J. Veverka, L. A. Soderblom, R. Beebe, J. Boyce, G. Briggs, M. Carr, S. A. Collins, A. F. Cook, G. E. Danielson, M. E. Davies, G. E. Hunt, A. Ingersol, T. V. Johnson and H. Masursky 1979a. The Galilean satellites and Jupiter: Voyager 2 imaging science results. *Science* 206, 927-50.

Smith, B. A., L. A. Soderblom, T. V. Johnson, A. P. Ingersoll, S. A. Collins, E. M. Shoemaker, G. E. Hunt, H. Masursky, M. H. Carr, M. E. Davies, A. F. Cook, II, J. Boyce, G. E. Danielson, T. Owen, C. Sagan, R. F. Beebe, J. Vevenca, R. G. Strom, J. F. McCauley, D. Morrison, G. A. Briggs and V. E. Suomi 1979b. The Jupiter system through the eyes of Voyager 1. *Science* 204, 951-7, 960-72.

Spencer, J. R. and N. M. Schneider 1996. Io on the eve of the Galileo mission. *Ann. Rev. Earth Planet. Sci.* 24, 125-190.

Stansberry, J. A., J. R. Spencer, R. R. Howell, C. Dumas and D. Vakil 1997. Violent silicate volcanism on Io in 1996. *Geophys. Res. Lett.* 24, 2455-8.

Tackley, P. J., D. J. Stevenson, G. A. Glatzmaier and G. Schubert 1993. Effects of an endothermic phase transition at 670 km depth in a spherical model of convection in the Earth's mantle. *Nature* 361, 699-704.

Tackley, P. J., D. J. Stevenson, G. A. Glatzmaier and G. Schubert 1994. Effects of multiple phase transitions in a 3-dimensional spherical model of convection in Earth's mantle. *J. Geophys. Res.* 99, 15877-15901.

Thomas, P. C., M. E. Davies, T. R. Colvin, J. Oberst, P. Schuster, G. Neukum, M. H. Carr, A. McEwen, G. Schubert and M. J. S. Belton 1998. The shape of Io from Galileo limb measurements. *Icarus* 135, 175-80.

Travis, B. and P. Olson 1994. Convection With Internal Heat-Sources and Thermal Turbulence In the Earths Mantle. *Geophysical Journal International* 118, 1-19.

Veeder, G. J., D. L. Matson, T. V. Johnson, D. L. Blaney and J. D. Goguen 1994. Io's heat flow from infrared radiometry, 1983-1993. *Journal of Geophysical Research, E, Planets* 99, 17,095-17,162.

Vincent, A. P. and D. A. Yuen 1999. Transition to turbulent thermal convection beyond Ra=10^10 detected in numerical simulations. *Phys. Rev. E* in press,

Yoder, C. F. 1979. How tidal heating in Io drives the Galilean orbital resonance locks. *Nature (UK)* 279, 767-70.

Yoder, C. F. and S. J. Peale 1981. The tides of Io. *Icarus* 47, 1-35.

Yuen, D. A., U. Hansen, W. Zhao, A. P. Vincent and A. V. Malevsky 1993. Hard Turbulent Thermal-Convection and Thermal Evolution Of the Mantle. *Journal Of Geophysical Research-Planets* 98, 5355-5373.

FIGURE CAPTIONS

Figure 1. Azimuthal distribution of heating for (a.) asthenosphere and (b.) mantle models, based on (Segatz *et al*. 1988, Ross *et al.* 1990). The sub- and anti-Jovian points correspond to 0° and 180° respectively. (c.) The radial distribution of mantle (blue line) and asthenosphere (red line) heating. In this plot each line is normalized to have a maximum of 1.

Figure 2. Isosurfaces of residual temperature for cases 1-4 with either mantle heating or asthenospheric heating. The central point in the image is at latitude 30° N, longitude 20° E. Blue isosurfaces show where the temperature is the specified amount lower than the geotherm, red isosurfaces show where it is higher than the geotherm. Contoured value is scaled by the standard deviation of the temperature field as follows: (a. b.) Mantle heating, Ra_H=2.5x10^4, isosurfaces

±266K, (c. d.), Asthenospheric heating, Ra_H=2.5x10^4, isosurfaces ±136K, (e. f.) Mantle heating Ra_H=2.5x10^7, isosurfaces ±70K (g. h.) Asthenospheric heating. Ra_H=2.5x10^7, isosurfaces ±70 K.

Figure 3. Temperature slices for various cases with mantle Ra_H=2.5x10^7. Pole-to pole slices at longitude=0 (far right in Figure 1) (a. c. i. k.), equatorial slices (b. d. j. l.), and constant-radius sections at mid-asthenospheric depth (e. g. m. o.) and mid-mantle depth (f. h. n. p.). On the constant-radius sections, the central point in the image is at latitude 30° N, longitude 20°. (a. b. e. f.) Case 2, all-mantle heating, temperature range 100-2200 K. (c. d. g. h.) Case 4, with all-asthenospheric heating, temperature range 100-1900 K. (i. j. m. n.) Case 8, with combined heating, temperature range 100-1900 K. (k. l. o. p.) Case 10, with combined heating and an impermeable asthenosphere-mantle boundary, temperature range 100-2400 K.

Figure 4. Isosurfaces of residual temperature for cases 5-8 with combined heating and mantle Ra_H increasing by factors of 10. Blue isosurfaces show where the temperature is the specified amount lower than the geotherm, red isosurfaces show where it is higher than the geotherm. Contoured value is scaled by the standard deviation of the temperature field as follows: (a. b.) Ra_H=2.5x10^4, isosurfaces ±145K, (c. d.), Ra_H=2.5x10^5, isosurfaces ±104K, (e. f.) Ra_H=2.5x10^6, isosurfaces ±73K (g. h.) Ra_H=2.5x10^7, isosurfaces ±50 K.

Figure 5. Isosurfaces of residual temperature for cases 9,10, and 11, with combined heating and various physical characteristics. Blue is colder than the geotherm, whereas red is hotter than the geotherm. Contoured value is scaled by the standard deviation as follows: (a. b.) impermeable A-M boundary, Ra_H=2.5x10^6, ±95 K, (c. d.) impermeable A-M boundary, Ra_H=2.5x10^7, ±100 K, (e. f.) permeable A-M boundary but asthenosphere same viscosity as mantle, Ra_H=2.5x10^7, ±83 K

Figure 6. Temperature profiles (geotherms) for the five Ra_H=2.5x10^7 cases 2, 4, 8, 10 and 11.

Figure 7. Variations in surface, base of lithosphere and CMB heat flux for cases 5-8 with combined heating, a permeable asthenosphere-mantle boundary, and Ra_H increasing in factors of 10 from 2.5x10^4 (top row) to 2.5x10^7 (bottom row). The color bar is in W/m^2.

Figure 8. Variations in surface, base of lithosphere and CMB heat flux for cases 2, 4, 10, and 11 with mantle Ra_H=2.5x10^7 and all-mantle heating (top row), all-asthenospheric heating (2nd row), combined heating with an impermeable mantle-asthenosphere boundary (3rd row), and combined heating with an asthenospheric viscosity equal to mantle viscosity (bottom row).

Figure 9. Scaling of rms. and peak-to-peak heat flux variation for cases 5-8 with combined heating and a permeable mantle-asthenosphere boundary.

Figure 10. Global distribution maps for volcanic centers (top) and mountains (bottom) on Io. Shown is the areal density in units of 10^6 km^{-2}. A strong anti-correlation between global distribution of volcanic centers and mountains is apparent. Values were determined by measuring the number of volcanic centers or mountains within a standard counting circle 15° in radius. Volcanic centers were defined as specific eruption sites, isolated lava flows, or individual volcanic constructs. Mountains were defined as contiguous non-erosional structures with positive relief exceeding ~1 km. Data are color-coded from blue (low) to red (high), with black indicating zero density. Areal density of volcanic centers ranges from 0 to 25.5 x 10^6 km^{-2}, and from 0 to 10 x10^6 km^{-2} for mountains (the low densities of volcanic centers are near the poles and could be incomplete due to oblique viewing geometry). Data are based on Voyager and Galileo nominal mission images (Schenk and Hargitai, 1998).

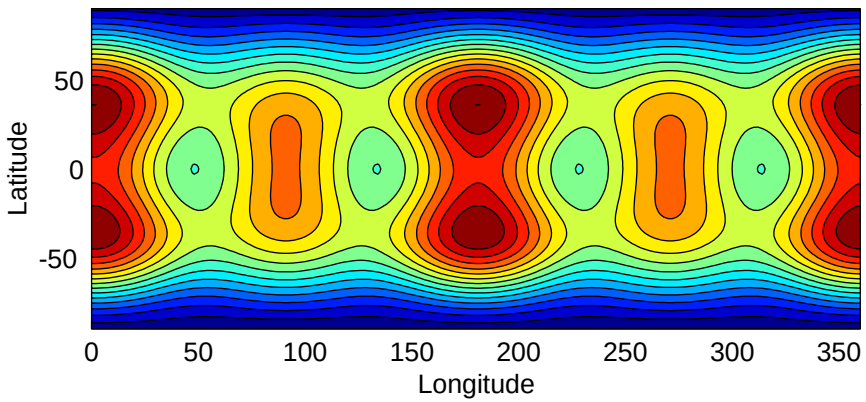
Latitude
50
0
-50
0
50
100
150
200
250
300
350
Longitude

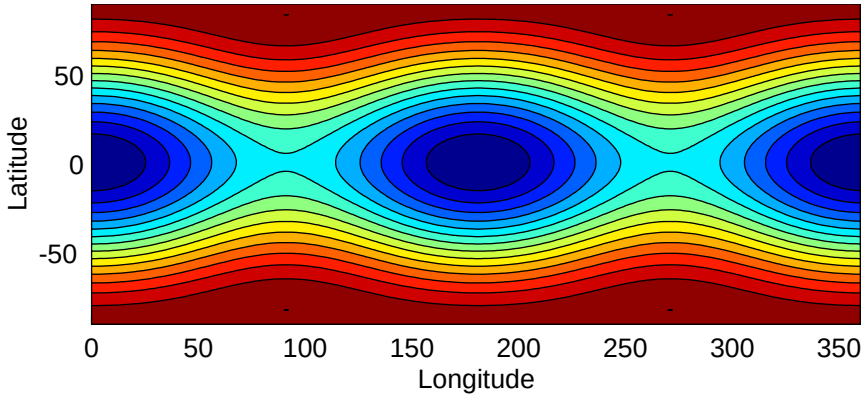
Latitude
50
0
-50
0
50
100
150
200
250
300
350
Longitude

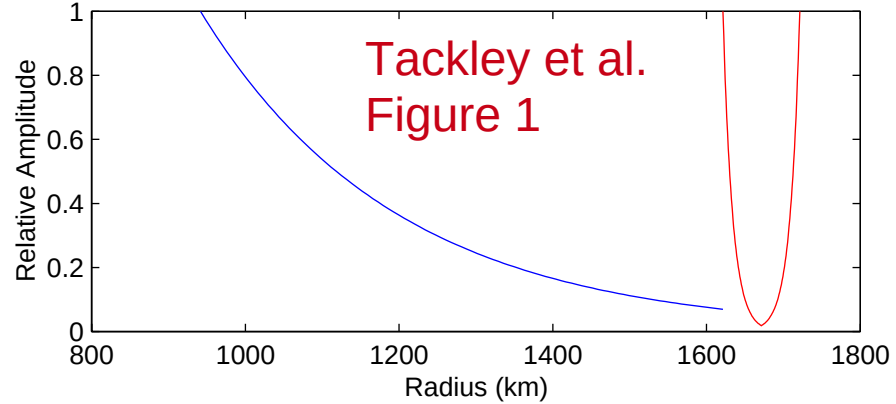
Tackley et al.
Figure 1
Relative Amplitude
1
0.8
0.6
0.4
0.2
0
800
1000
1200
1400
1600
1800
Radius (km)

Tackley et al. Figure 2

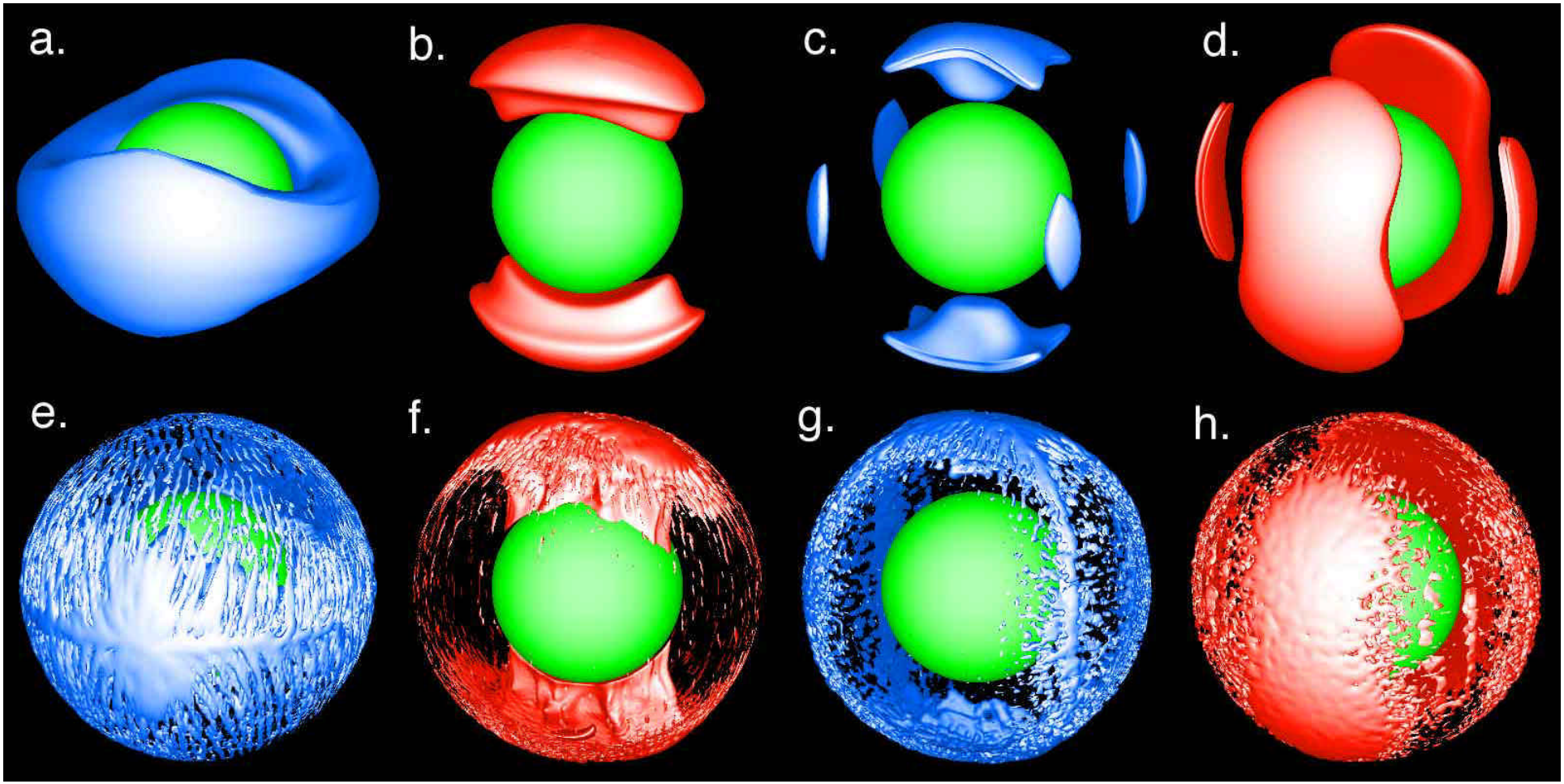

Tackley et al. Figure 3

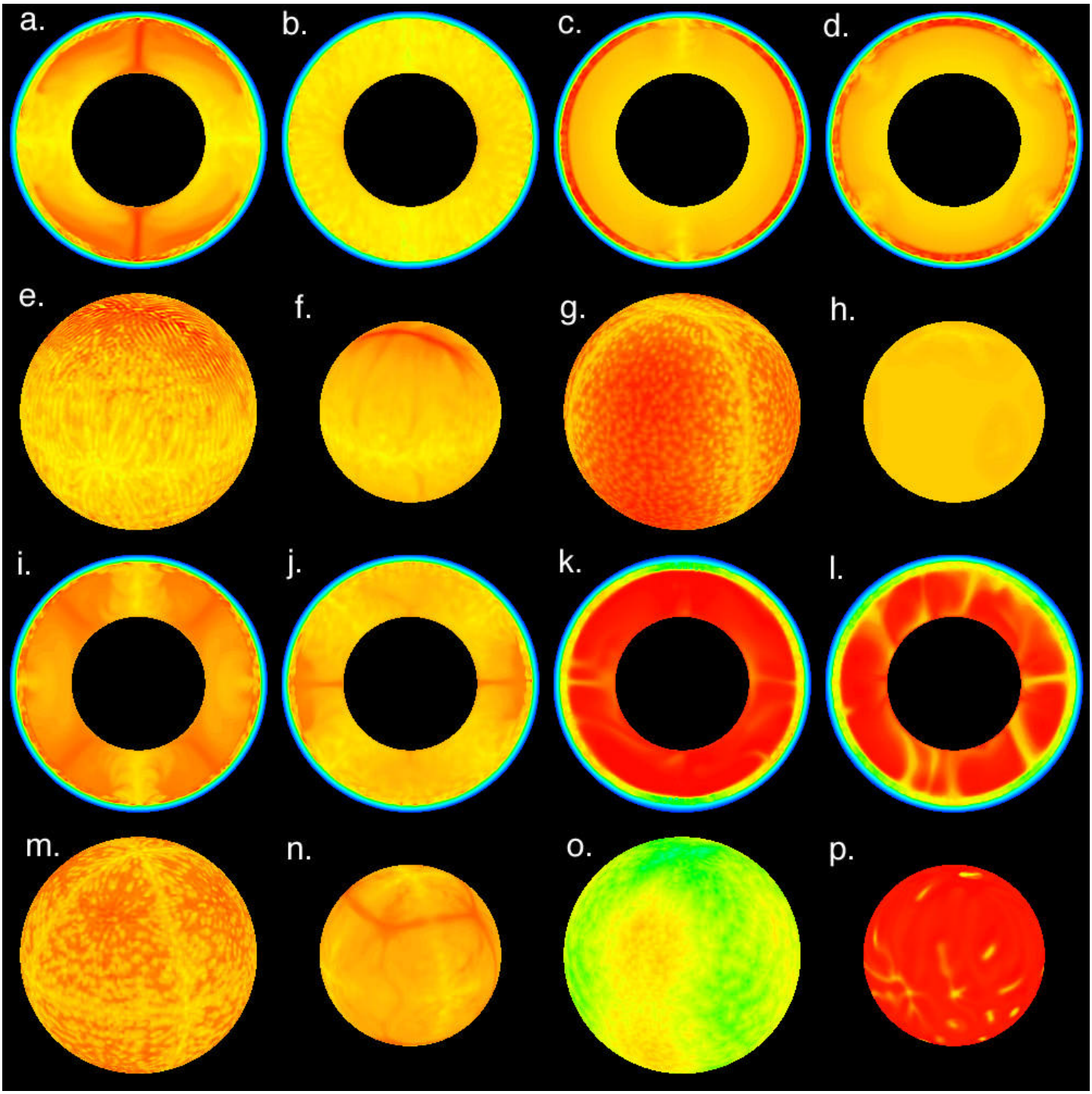

Tackley et al. Figure 4

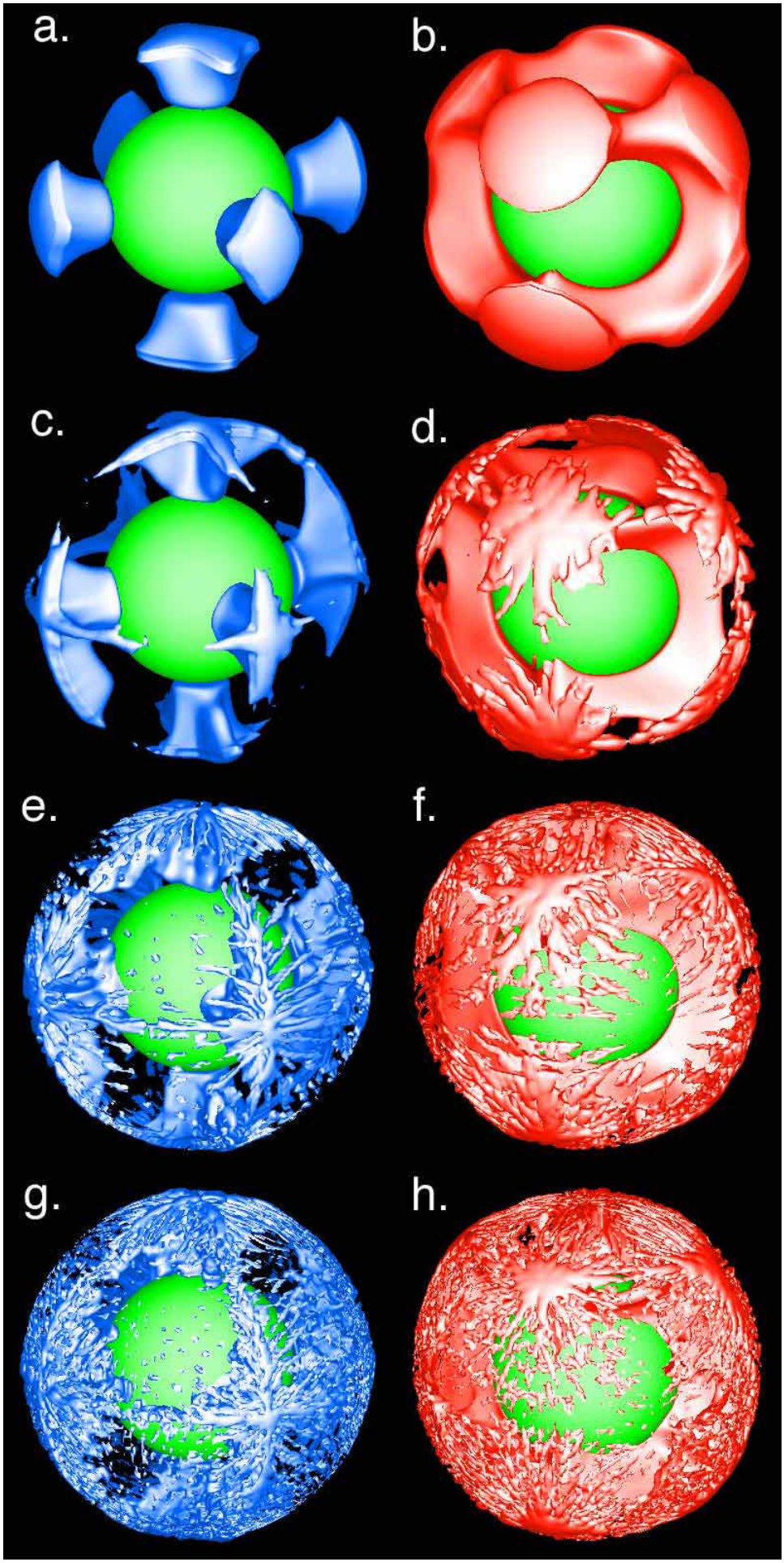

Tackley et al. Figure 5

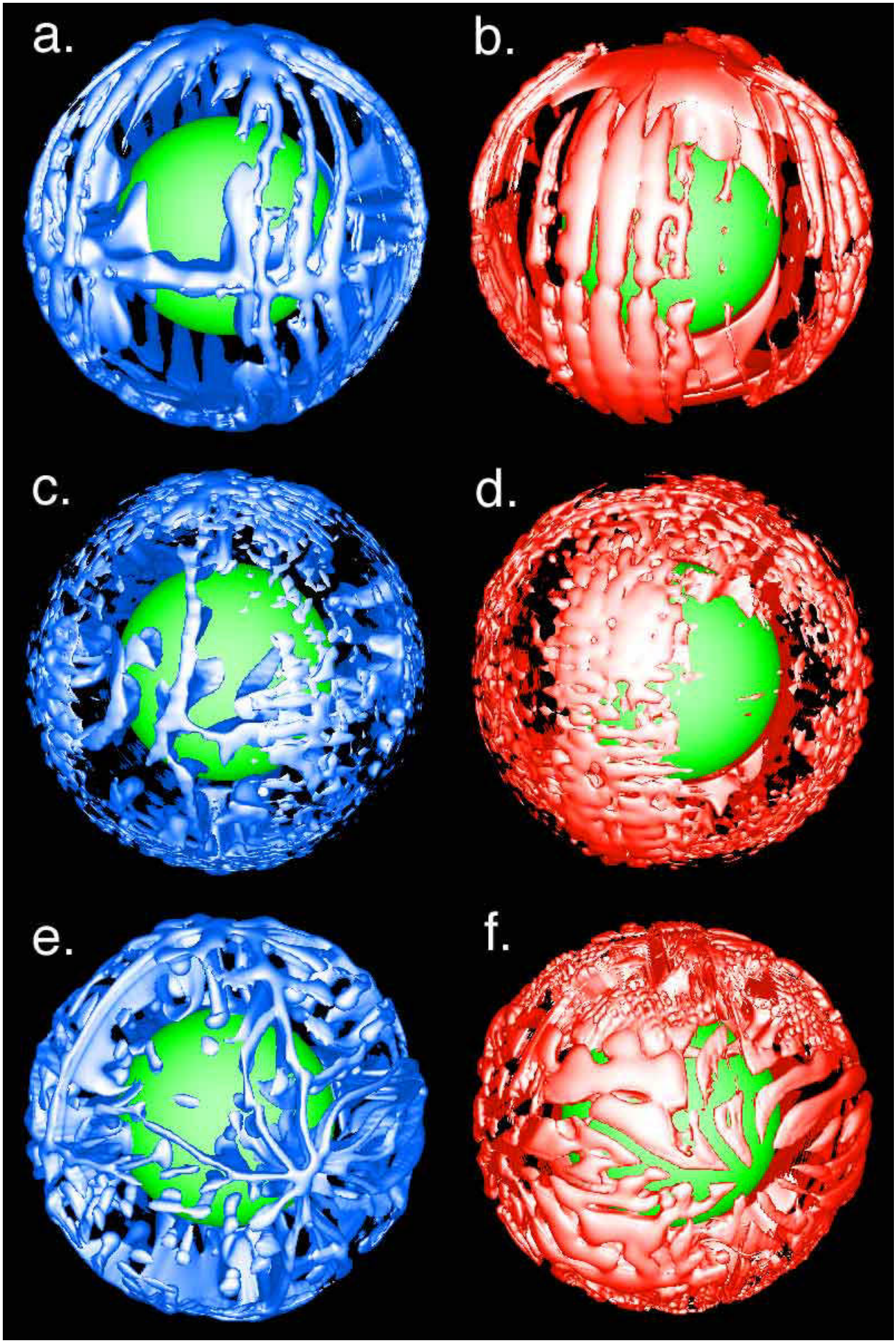

Tackley et al. Figure 6

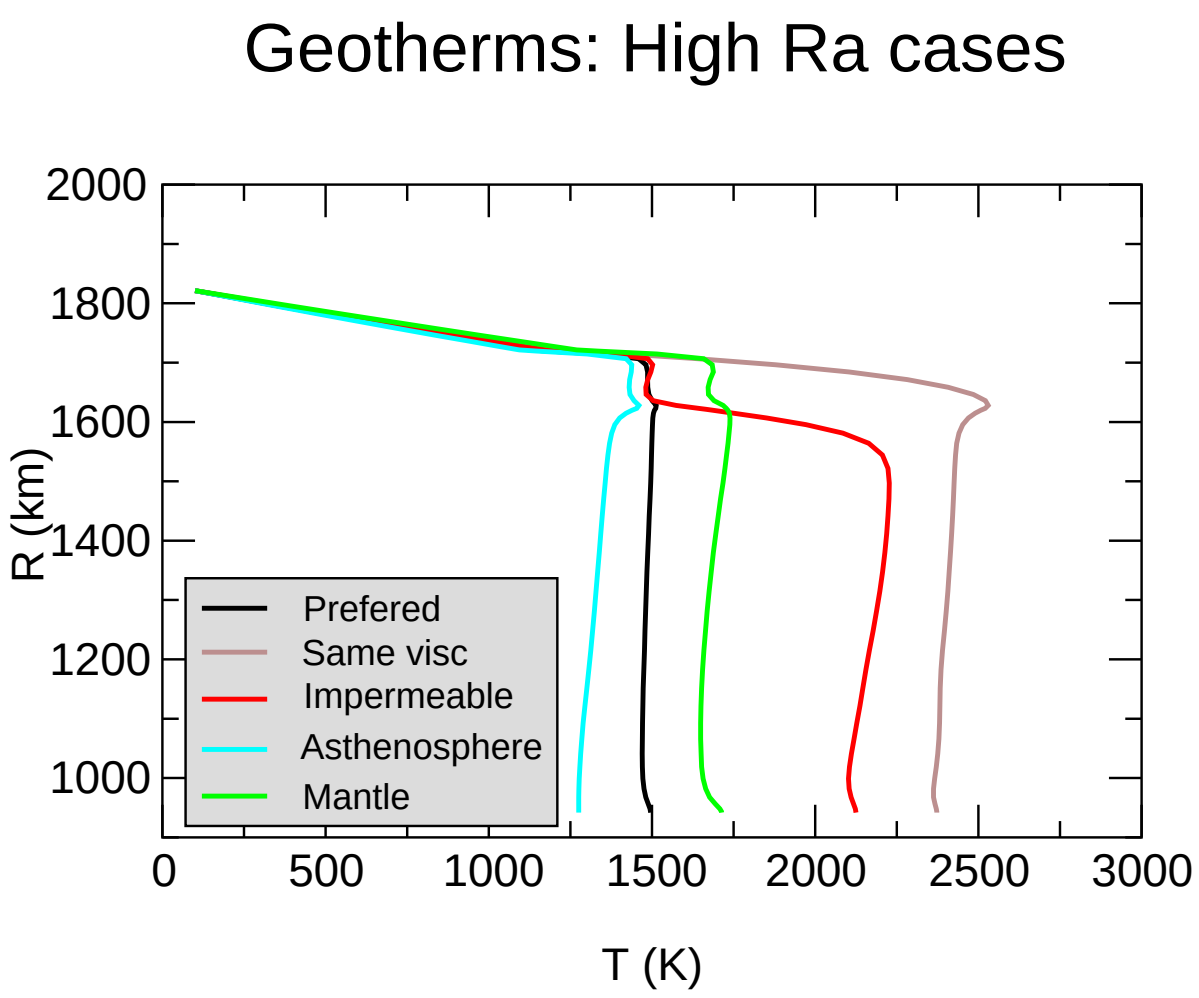

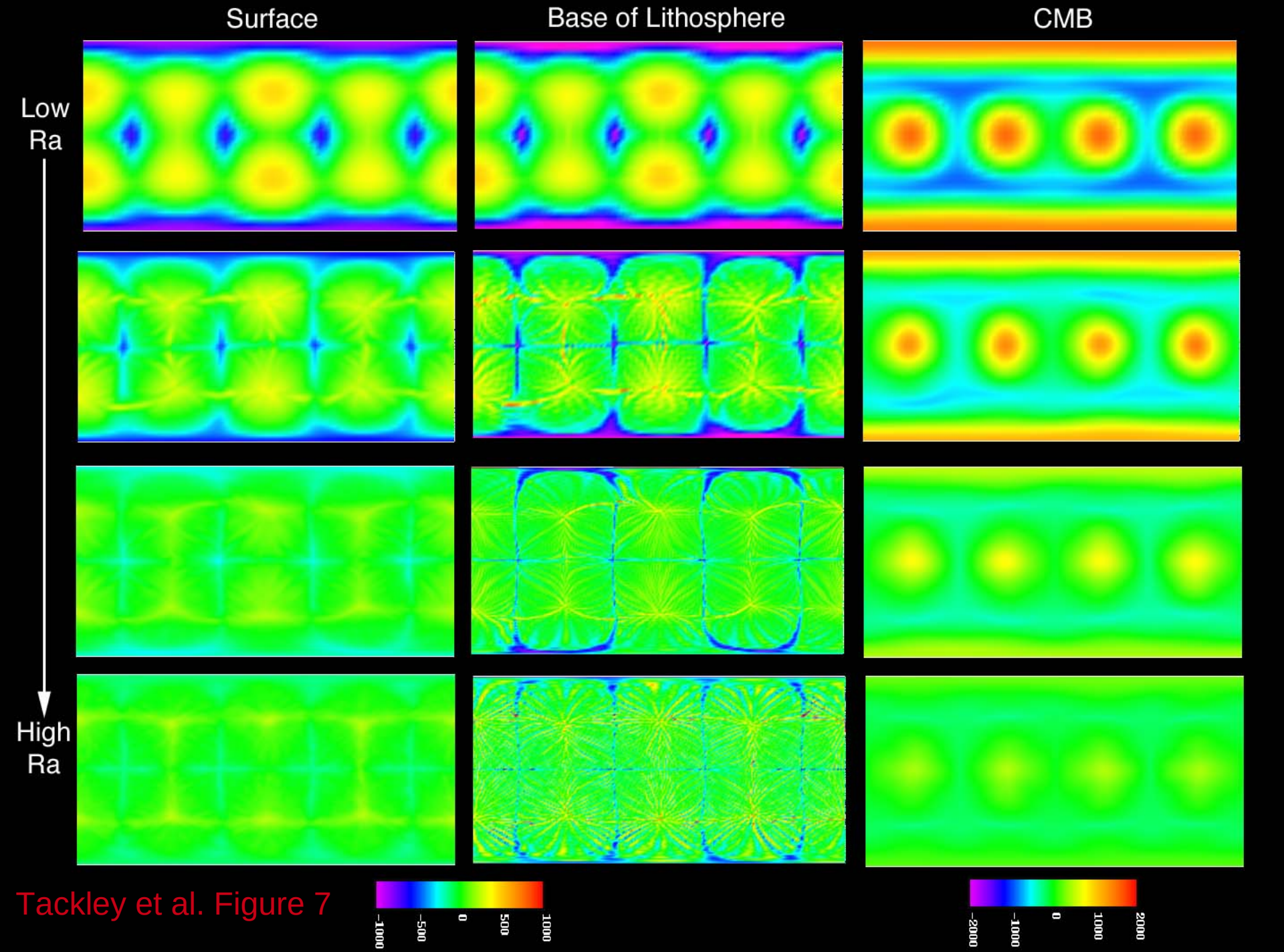

Tackley et al. Figure 7

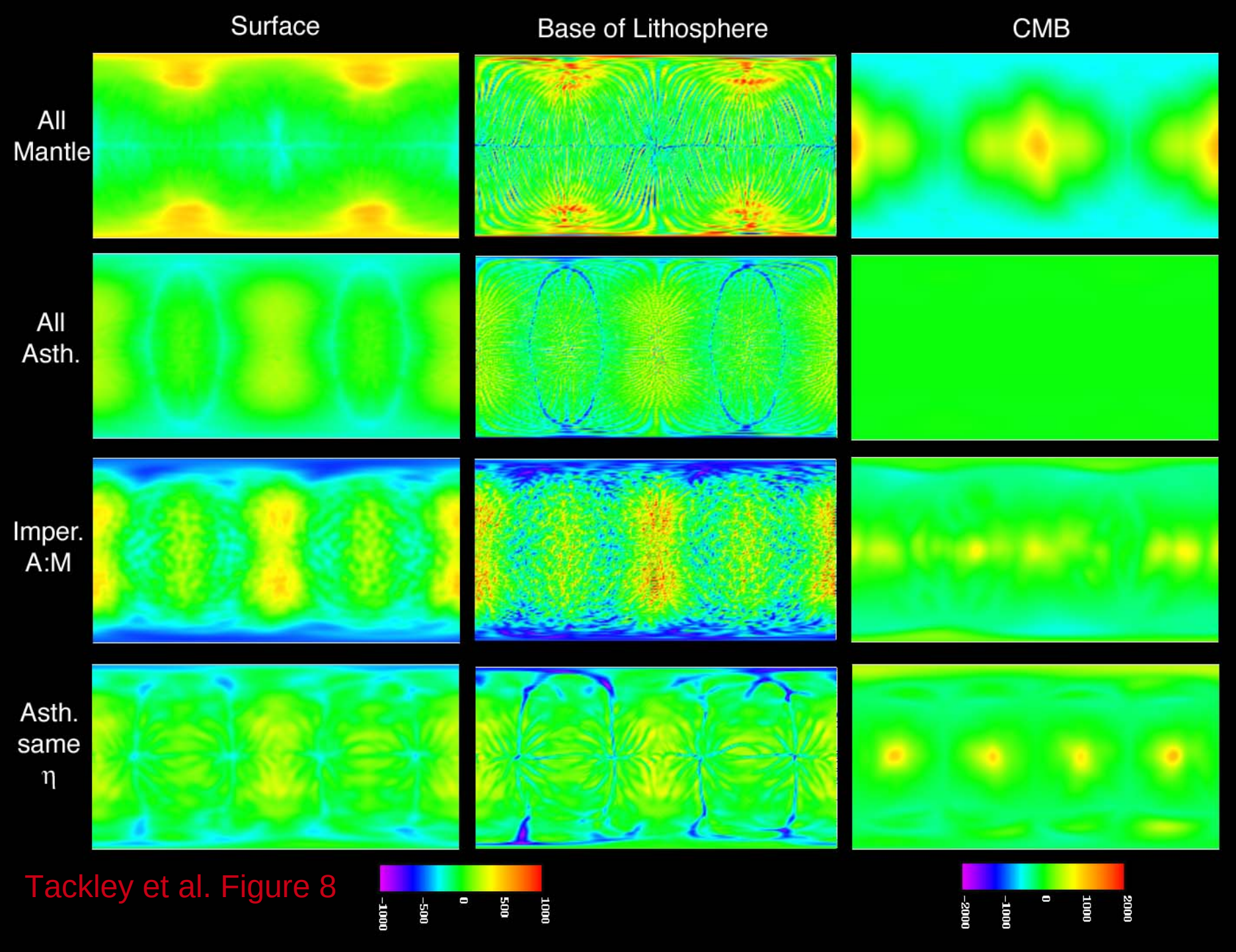

Tackley et al. Figure 8

Tackley et. al. Figure 9

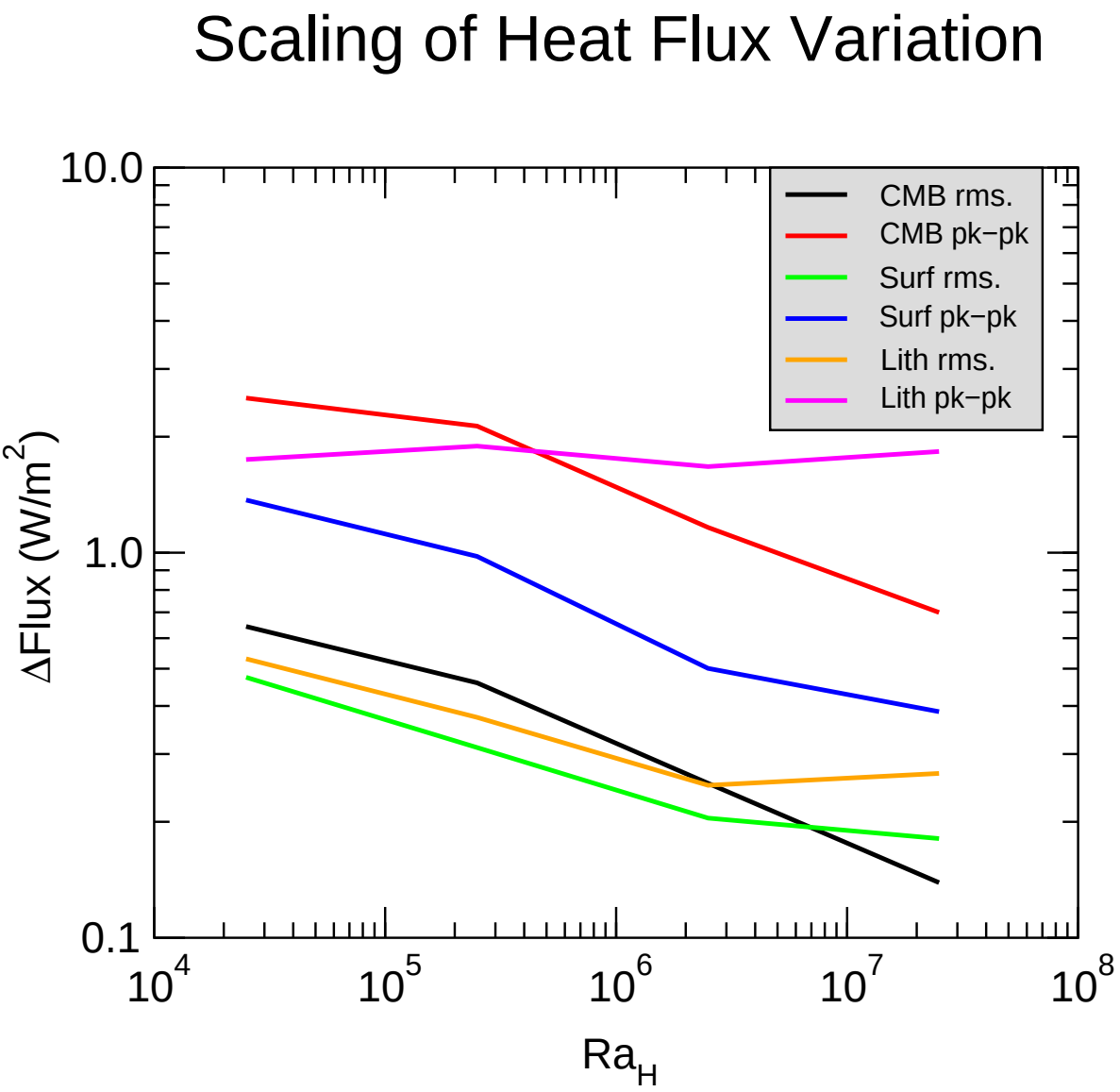

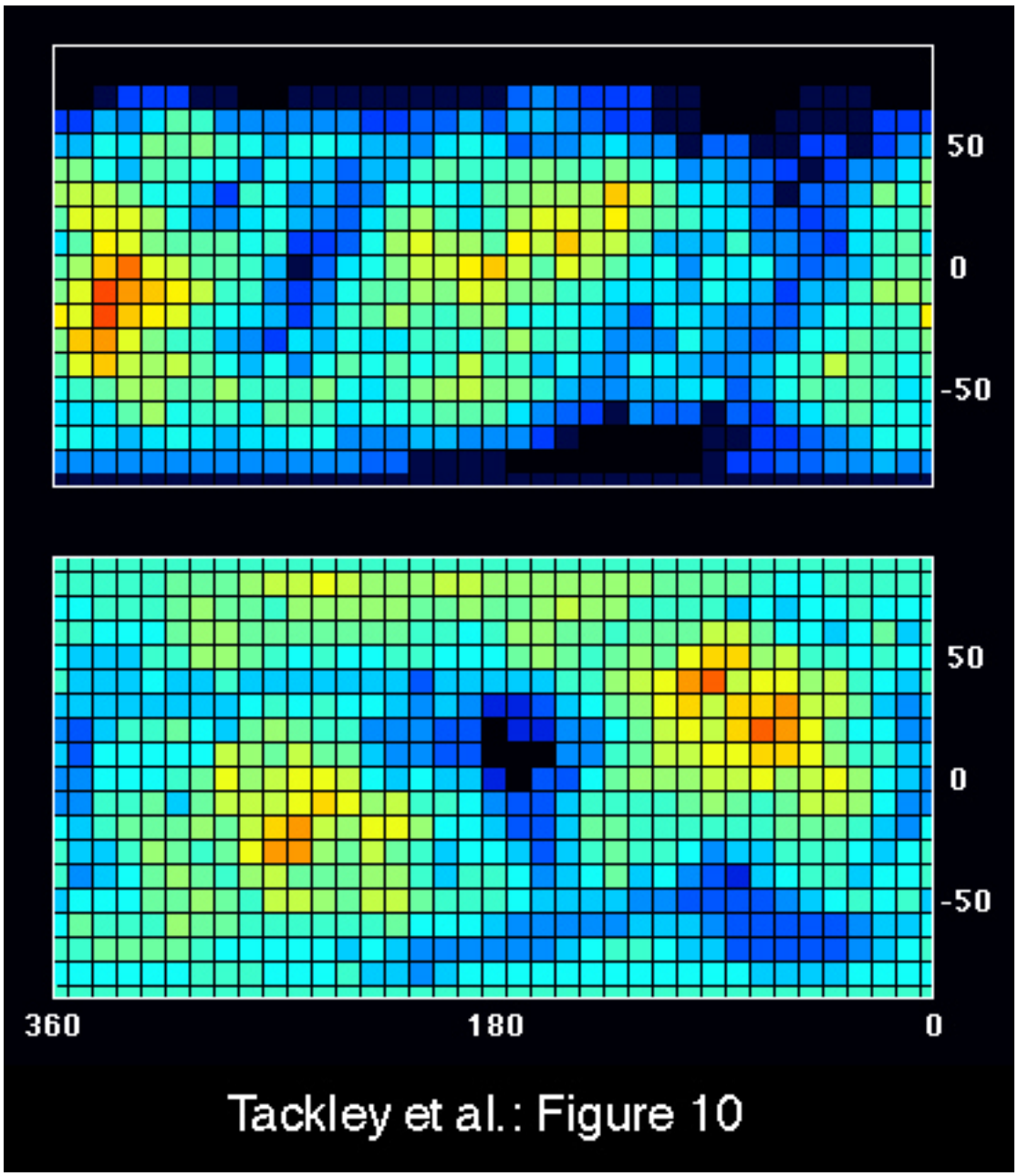

Tackley et al.: Figure 10